International Communications in Heat and Mass Transfer 39 (2012) 896–903

Contents lists available at SciVerse ScienceDirect

International Communications in Heat and Mass Transfer

journal homepage: www.elsevier.com/locate/ichmt

Laminar flow with combustion in inert porous media ☆

José E.A. Coutinho, Marcelo J.S. de Lemos *

Departamento de Energia, IEME, Instituto Tecnológico de Aeronáutica — ITA, 12228-900 São José dos Campos, S.P., Brazil

ARTICLE INFO

Available online 13 June 2012

Keywords:
Porous burners
Filtration combustion
Porous media

ABSTRACT

This work presents one-dimensional numerical results for combustion of an air/methane mixture in inert porous media using laminar and radiation models. Comparisons with experimental data are reported. The burner is composed by a preheating section followed by a combustion region. Macroscopic equations for mass, momentum and energy are obtained based on the volume average concept. Distinct energy equations are considered for the porous burner and the flowing gas. The numerical technique employed for discretizing the governing equations was the control volume method with a boundary-fitted non-orthogonal coordinate system. The SIMPLE algorithm was used to relax the entire equation set. Inlet velocity, excess air, porosity and solid-to-fluid thermal conductivity ratio were varied in order to investigate their effect on temperature profiles. Results indicate that higher inlet velocities result in higher gas temperatures, following a similar trend observed in the experimental data used for comparisons. Burning of mixtures close to the stoichiometric conditions also increased temperatures, as expected. Increasing the thermal conductivity of the preheating section reduced peak temperature in the combustion region. The use of porous material with very high thermal conductivity on the combustion region did not affect significantly temperature levels in the combustion section.

1 . Introduction

Combustion in inert porous media has been extensively investigated due to many engineering applications and demand for developing high-efficiency power production devices. The growing use of radiant burners can be encountered in the power and process industries and, as such, proper mathematical models of flow, heat and mass transfer in porous media with combustion can benefit the development of such equipment.

The advantages of having a combustion process inside porous matrix are today well documented in the open literature, including basic research for hydrocarbon fuels [1], applications aiming at internal combustion engines [2], use of low heating value fuels [3] as well as liquid fuels [4]. A recent view on using hydrogen/air mixtures for fuel cell applications has been also reported [5]. Recent reviews on the topic have also been recently published [6,7]. Hsu et al. [8] points out some of the benefits of porous burners, such as higher burning speed and volumetric energy release rates, higher combustion and flame stability, the ability to burn gases of low energy content, and many other advantages.

Previously, a systematic series of studies on flow in inert porous media was compiled and documented in a book [9]. Subsequently, in a series of papers, the thermo-mechanical model detailed in [9] was extended to include exothermic chemical reactions assuming thermal non-equilibrium between the solid matrix and the flowing gas [10,11]. In addition, simulations using local thermal equilibrium [12] as well as moving solid beds [13] were also reported. However, in all the theoretical and numerical work just mentioned, no comparison with experimental data was presented due to the scarcity of published data.

The objective of the present contribution is to report comparisons of the model in [10] with experimental data by Pereira [14], checking the correctness and accuracy of the thermo-mechanical model described in the above mentioned papers. Here, laminar flow is considered. Computations are carried out for inert porous material considering one-dimensional thermal fields and a two-energy equation model with radiation transport.

2 . Macroscopic mathematical model

As the macroscopic model is already available in the open literature [10–12], governing equations will be just presented. They can be summarized as follows:

2.1. Continuity equation

$$\nabla\cdot\rho_f \mathbf{u}_D = 0 \tag{1}$$

where $\mathbf{u}_D$ is the average surface velocity (also known as seepage, superficial or Darcy Velocity) and ρ_f is the fluid density. Eq. (1) represents the macroscopic continuity equation for the gas.

☆ Communicated by: W.J. Minkowycz.
* Corresponding author.
E-mail address: delemos@ita.br (M.JS. de Lemos).

0735-1933/$ – see front matter © 2012 Elsevier Ltd. All rights reserved.
doi:10.1016/j.icheatmasstransfer.2012.06.002

Nomenclature

Latin characters

A	Pre-exponential factor
a_i	Specific interfacial area
A_i	Interfacial area
c_F	Forchheimer coefficient
c_p	Specific heat
D	Mean particle diameter
$\mathbf{D}_{eff}$	Effective mass transport tensor
$\mathbf{D}_{diff}$	Mass diffusion transport tensor
$\mathbf{D}_{disp}$	Dispersion transport tensor
E	Activation Energy
h_i	Film coefficient for interfacial transport
K	Permeability
k	Thermal conductivity
$\mathbf{K}_{eff}$	Effective thermal conductivity tensor
$\mathbf{K}_{disp}$	Thermal dispersion tensor
m	Mass fraction
M	Molecular weight
$\mathbf{n}_i$	Normal unitary vector
p	Pressure of the fluid phase
P_0	Reference pressure
P_{den}	Pore linear density (ppcm)
Pr	Prandtl number
R	Universal gas constant
Re_D	Reynolds number based on D
Re_{in}	Reynolds number based on inlet mass flow rate
S_{fu}	Rate of fuel consumption
Sc	Schmidt number
T	Temperature
$\mathbf{u}$	Microscopic velocity
$\mathbf{u}_D$	Darcy or superficial velocity (volume average of $\mathbf{u}$)
u_{in}	Inlet velocity

Greek characters

β_r	Extinction coefficient
ΔV	Representative elementary volume
ΔV_f	Fluid volume inside ΔV
ΔH	Heat of combustion
ϕ	$\phi = {}^{\Delta V_f}/_{\Delta V}$, Porosity
μ	Dynamic viscosity
Ψ	Excess air-to-fuel ratio
ρ	Density
σ	Stephan–Boltzman constant

Special characters

φ	General variable
$\langle\varphi\rangle^i$	Intrinsic average
${}^i\varphi$	Spatial deviation
$()_{s,f}$	Solid/fluid phase
$()_\ell$	Related to species ℓ
$()_{fu}$	Fuel
$()_{ox}$	Oxidant

2.2. Momentum equation

$$\nabla\cdot\left(\rho_f\frac{\mathbf{u}_D\mathbf{u}_D}{\phi}\right)=-\nabla\left(\phi\langle p\rangle^i\right)+\mu\nabla^2\mathbf{u}_D-\left[\frac{\mu\phi}{K}\mathbf{u}_D+\frac{c_F\phi\,\rho_f|\mathbf{u}_D|\mathbf{u}_D}{\sqrt{K}}\right] \quad (2)$$

where the last two terms in Eq. (2) represent the Darcy and Forchheimer contributions. The symbol K is the porous medium permeability, $c_F = 0.55$ is the form drag coefficient, $\langle p\rangle^i$ is the intrinsic average pressure of the fluid phase, ρ_f is the fluid density, μ represents the fluid viscosity and ϕ is the porosity of the porous medium. The permeability K of the porous matrix is determined using the Ergun [15] equation,

$$K=\frac{\phi^3\cdot D^2}{144\cdot(1-\phi)} \quad (3)$$

where D in the particle diameter.

2.3. Two-energy equation model

When average temperatures in distinct phases are substantially different from each other, for example in combustion processes, macroscopic energy equations are obtained for both fluid and solid phases by applying time and volume average operators to the instantaneous local equations [16,17]. We name this approach Local Thermal Non Equilibrium model (LTNE). After including the heat released due to the combustion reaction, one gets for both phases:

$$\text{Gas}: \nabla\cdot\left(\rho_f c_{pf}\mathbf{u}_D\langle T_f\rangle^i\right)=\nabla\cdot\left\{\mathbf{K}_{eff,f}\cdot\nabla\langle T_f\rangle^i\right\}+h_i a_i\left(\langle T_s\rangle^i-\langle T_f\rangle^i\right)+\phi\Delta H S_{fu} \quad (4)$$

$$\text{Solid}: 0=\nabla\cdot\left\{\mathbf{K}_{eff,s}\cdot\nabla\langle T_s\rangle^i\right\}-h_i a_i\left(\langle T_s\rangle^i-\langle T_f\rangle^i\right) \quad (5)$$

where, $a_i = A_i/\Delta V$ is the interfacial area per unit volume, h_i is the film coefficient for interfacial transport, $\mathbf{K}_{eff,f}$ and $\mathbf{K}_{eff,s}$ are the effective conductivity tensors for fluid and solid, respectively, given by:

$$\mathbf{K}_{eff,f}=\left\{\overbrace{\phi k_f}^{\text{conduction}}\right\}\mathbf{I}+\underbrace{\mathbf{K}_{f,s}}_{\text{localconduction}}+\underbrace{\mathbf{K}_{disp}}_{\text{dispersion}} \quad (6)$$

$$\mathbf{K}_{eff,s}=\left\{\overbrace{(1-\phi)\left[k_s+\frac{\overbrace{16\sigma\left(\langle T_s\rangle^i\right)^3}^{\text{radiation}}}{3\beta_r}\right]}^{\text{conduction}}\right\}\mathbf{I}+\underbrace{\mathbf{K}_{s,f}}_{\text{local conduction}}. \quad (7)$$

In Eqs. (4) to (7), $\mathbf{I}$ is the unit tensor, ΔH is the heat of combustion, β_r is the extinction coefficient, $\sigma = 5.66961\times10^{-8}\ \mathrm{W/m^2K^4}$ is the Stephan–Boltzman constant and S_{fu} is the rate of fuel consumption, to be commented below. In Eqs. (4) and (5) all mechanisms contributing to heat transfer within the medium, together with radiation transport, are included in order to compare their effect on temperature distribution. Further, distinct contributions of various mechanisms come from applying gradient type diffusion models, in the form:

$$\text{Thermal dispersion}: -\left(\rho c_p\right)_f\left(\phi\,\langle{}^i\mathbf{u}^i T_f\rangle^i\right)=\mathbf{K}_{disp}\cdot\nabla\langle T_f\rangle^i \quad (8)$$

$$\text{Local conduction}:\begin{cases}\nabla\cdot\left[\dfrac{1}{\Delta V}\displaystyle\int_{A_i}\mathbf{n}_i k_f T_f\ dA\right]=\mathbf{K}_{f,s}\cdot\nabla\langle T_s\rangle^i\\ -\nabla\cdot\left[\dfrac{1}{\Delta V}\displaystyle\int_{A_i}\mathbf{n}_i k_s T_s\ dA\right]=\mathbf{K}_{s,f}\cdot\nabla\langle T_f\rangle^i\end{cases}. \quad (9)$$

Further, in Eqs. (4) and (5), the heat transferred between the two phases was modeled by means of a film coefficient h_i. A numerical

correlation for the interfacial convective heat transfer coefficient was proposed by Kuwahara et al. [18], for laminar flow, as:

$$\frac{h_i D}{k_f} = \left(1 + \frac{4(1-\phi)}{\phi}\right) + \frac{1}{2}(1-\phi)^{1/2}\mathrm{Re}_D \mathrm{Pr}^{1/3}, \tag{10}$$

valid for $0.2 < \phi < 0.9$

where Re_D is the Reynolds number based on D and the macroscopically uniform velocity, $\mathbf{u}_D$, given by:

$$\mathrm{Re}_D = \frac{\rho_f |\mathbf{u}_D| D}{\mu}. \tag{11}$$

2.4. Mass transport equation

Transport equation for the volume-averaged fuel mass fractions $\langle m_{fu}\rangle^i$ reads:

$$\nabla\cdot\left(\rho_f \mathbf{u}_D \langle m_{fu}\rangle^i\right) = \nabla\cdot\rho_f \mathbf{D}_{eff}\cdot\nabla\left(\phi\langle m_{fu}\rangle^i\right) - \phi S_{fu} \tag{12}$$

where the effective mass transport tensor $\mathbf{D}_{eff}$ is defined as:

$$\mathbf{D}_{eff} = \underbrace{\mathbf{D}_{disp}}_{\text{dispersion}} + \overbrace{\mathbf{D}_{diff}}^{\text{diffusion}} = \mathbf{D}_{disp} + \frac{1}{\rho_f}\left(\frac{\mu_\phi}{Sc_\ell}\right)\mathbf{I} \tag{13}$$

and Sc_ℓ is the laminar Schmidt number of species ℓ. The dispersion tensor is defined such that,

$$-\rho_f \phi \langle {}^i\mathbf{u}\, {}^i m_{fu}\rangle^i = \rho_f \mathbf{D}_{disp}\cdot\nabla\left(\phi\langle m_{fu}\rangle^i\right). \tag{14}$$

2.5. One-step global mechanism

In this work, for simplicity, the chemical exothermic reaction is assumed to be instantaneous and to occur in a single step, kinetic-controlled, which, for combustion of a mixture air/methane, is given by the chemical reaction [19,20]:

$$CH_4 + 2(1+\Psi)(O_2 + 3.76N_2) \rightarrow CO_2 + 2H_2O + 2\Psi O_2 + 7.52(1+\Psi)N_2 \tag{15}$$

where Ψ is the excess air in the reactant stream at the inlet of the porous foam. For the stoichiometric condition, $\Psi = 0$. As mentioned, the reaction is assumed to be kinetically controlled and occurring infinitely fast.

The local instantaneous rate of fuel consumption over the total volume (fluid plus solid) was determined by a one-step Arrhenius reaction [20], given by:

$$S_{fu} = \rho_f^a A \langle m_{fu}^b\rangle^i \langle m_{ox}^c\rangle^i e^{-E/R\langle T_f\rangle^i} \tag{16}$$

where $\langle m_{fu}\rangle^i$ and $\langle m_{ox}\rangle^i$ are the volume averaged mass fractions for the fuel and oxidant, respectively, and coefficients a, b and c depend on the particular reaction [21]. We assume here $a=2$, $b=c=1$, which corresponds to the burning of a mixture composed by methane and air [20]. Also, in Eq. (16), A is the pre-exponential factor and E is the activation energy, where numerical values for these parameters depend on the fuel considered [22].

The gas density ρ_f in the above equations is determined from the perfect gas equation for a mixture of perfect gases:

$$\rho_f = \frac{P_o}{RT_f \sum_1^\ell \frac{m_\ell}{M_\ell}} \tag{17}$$

where P_o is a reference pressure, $R = 8.134$ J/(mol.kg) is the universal gas constant and M_ℓ is the molecular weight of species ℓ.

3 . Results and discussion

3.1. Geometry and cases investigated

For validating the code, we compared simulations herein with experimental values reported by Pereira (2002) [14]. There, the burning device was described as consisting of four commercial ceramic filters mounted as depicted in Fig. 1. Each of the four filters was 70 mm in diameter and had a length of 20 mm. Further, the apparatus described in [14] was composed by two regions. First, a preheating section with $\phi = 0.86$ and $P_{den} = 15.74$, where P_{den} or "ppcm" is the number of pores per linear centimeter, preceded a combustion region with $\phi = 0.9$ and $P_{den} = 3.9$. In addition, in order to determine the value of particle diameter D to be used in Eq. (3) to calculate the permeability K, which was not available in [14] but is needed to solve the momentum Eq. (2), the particle diameter was determined from the following expression:

$$D = \frac{300}{P_{den}}\cdot\sqrt{\frac{(1-\phi)^2}{\phi\pi}}. \tag{18}$$

In Eq. (18), P_{den}, as mentioned, is the number of pores per centimeters (ppcm) and D is calculated in meters. Expression (18) can be easily deduced if one assumes that the porous medium is modeled as a regularly stacked square array of spheres of diameter D.

Also, measurements in [14] were taken with three sets of nine thermocouples each, displaced along the burner and located 120° apart, in the tangential direction, following a line distant 5 mm from the burner wall (dashed line in Fig. 1). The experimental values for temperatures plotted below represent the average, in each axial position, of the three thermocouples positioned in the same cross-section of the burner. The error bars below are associated with the maximum temperature difference, at each longitudinal position, among the three measurements taken at each r-θ plane.

Here, the values for the parameters in Eq. (16) were taken from Hanamura et al. [23] and are $E = 1.3\times10^5$ J/mol and $A = 2.6\times10^8$ s^{-1}. For methane, the heat of combustion is giving in the literature as $\Delta H = 5.0\times10^7$ J/kg. However, because heat losses due to conduction and convection were reported by [14], a lower value for ΔH is here employed to accommodate the fact that some generated heat was lost to the environment. In the simulations to follow, $\Delta H = 4.5\times10^7$ J/kg,

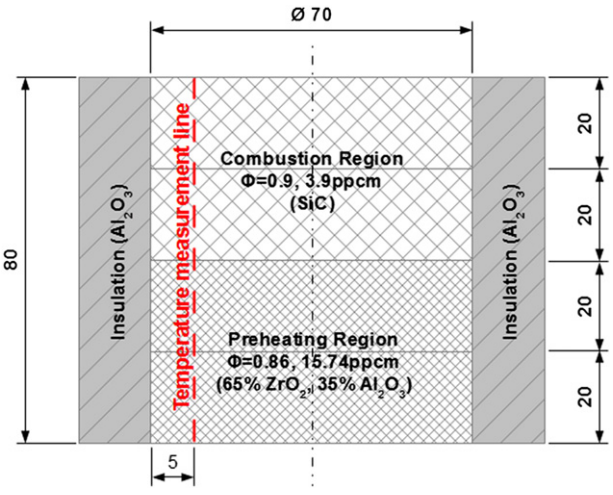

Fig. 1. Schematic of the burner projected by Pereira [14], dimensions in millimeters (mm).

or a 10% loss is considered. Further, simulations are assumed to be one-dimensional along the axial burner. Table 1 summarizes the cases presented in reference [14] as well as the numerical values used in the present work. For simulations, overall residuals for all transported variables were brought down to 10^{-10} before convergence was assumed to be achieved.

Table 1
Values used and cases investigated.

Cases investigated		u_{in} [m/s]	Re_{in}	Re_D	Ψ	Preheating region $K=5.93\times10^{-9}$ m^2 (fixed) $D=1.62\times10^{-4}$ m (except in Fig. 5a)			Combustion region $K=1.04\times10^{-7}$ m^2 (fixed) $D=4.53\times10^{-4}$ m (except in Fig. 5b)		
						ϕ	P_{den}[ppcm]	k_s/k_f	ϕ	P_{den}[ppcm]	k_s/k_f
Validation, Pereira [14]	Case 01	0.15	667.90	1.55	1.00	0.86	15.75	392.16	0.90	3.94	3529.41
	Case 02	0.21	935.05	2.17							
	Case 03	0.40	1780.50	4.13	0.67			391.74			3525.62
Effect of u_{in}, Fig. 4a		0.05	222.56	0.52	0.67	0.86	15.75	391.74	0.90	3.94	3525.62
		0.10	445.13	1.03							
		0.15	667.90	1.55							
		0.20	890.25	2.06							
		0.25	1112.81	2.58							
		0.30	1335.38	3.10							
		0.35	1557.94	3.61							
		0.40	1780.50	4.13							
		0.45	2003.06	4.64							
		0.50	2225.63	5.16							
Effect Ψ, Fig. 4b		0.40	1780.50	4.13	0.82	0.86	15.75	391.95	0.90	3.94	3527.51
					0.67			391.74			3525.62
					0.54			391.53			3523.75
					0.43			391.32			3521.89
					0.33			391.12			3520.04
					0.25			390.91			3518.20
					0.18			390.71			3516.38
					0.11			390.51			3514.56
					0.05			390.31			3512.76
					0.00			390.11			3510.97
Effect of ϕ in the preheating region, Fig. 5a		0.40	1780.50	33.25	0.67	0.50	9.16	391.74	0.90	3.94	3525.62
				25.94		0.55	10.07				
				20.23		0.60	10.99				
				15.70		0.65	11.90				
				12.04		0.70	12.82				
				9.05		0.75	13.73				
				6.57		0.80	14.65				
				4.50		0.85	15.56				
				2.73		0.90	16.48				
				1.27		0.95	17.40				
Effect of ϕ in the combustion region, Fig. 5b		0.40	1780.50	4.13	0.67	0.86	15.75	391.74	0.50	2.19	3525.62
									0.55	2.41	
									0.60	2.62	
									0.65	2.84	
									0.70	3.06	
									0.75	3.28	
									0.80	3.50	
									0.85	3.72	
									0.90	3.94	
									0.95	4.16	
Effect of k_s/k_f in the preheating region, Fig. 6a		0.40	1780.50	4.13	0.67	0.86	15.75	195.87	0.90	3.94	3525.62
								391.74			
								783.47			
								1175.21			
								1566.94			
								1958.68			
								2938.02			
								3917.36			
								4896.70			
								5876.04			
Effect of k_s/k_f in the combustion region, Fig. 6b		0.40	1780.50	4.13	0.67	0.86	15.75	391.74	0.90	3.94	1566.94
											1958.68
											2350.42
											2742.15
											3133.89
											3525.62
											3917.36
											4896.70
											5876.04
											7834.72

3.2. Grid independency studies

Mesh independency studies were carried out for several one-dimensional grids, with sizes spanning form 100 to 997 nodes along the axial direction of the burner of Fig. 1. Fig. 2 presents results for the gas and solid temperature for different meshes. Cases in Fig. 2 use values for excess air Ψ and inlet velocity u_{in} corresponding to the three cases reported by [14] (see Table 1). It is interesting to note in the figure that for grids with less than 400 nodes and for Cases 01 (Fig. 2*a*) and 02 (Fig. 2*b*), no ignition was obtained, or say, temperature profiles stay flat, reproducing along the burner the same temperature given at inlet (lines with square symbols). Also noted is that for grids with more than 400 nodes, results for temperature vary of a small amount. Nevertheless, for the sake of numerical accuracy, all results below made use of the finest grid, which had 997 nodes along the axial direction.

3.3. Code validation

Once the grid was determined, aiming at reducing numerical inaccuracy of the results, comparisons with experimental values follow. Fig. 3 presents simulations for temperatures for the three cases presented by Pereira [14]. Rise of temperatures for an increase in power, or inlet mass flow rate, is correctly simulated when comparing Fig. 3*a* and *b*, being both figures run with $\Psi = 1$. Further increasing the inlet velocity, Fig. 3*c*, raises the power input further increasing temperatures, a feature also captured by the model above. At outlet, one can see that the drop of measured temperatures is here not well reproduced and that might be related to the inappropriateness of the applied boundary condition at the burner exit. Here, a pure radiation loss for the solid material was used at the end of the burner.

It is important to emphasize that location of the thermocouples did not correspond to the location of gas temperature peaks seen in Fig. 3. However, at the discrete locations of the thermocouples, which were 10 cm apart from each other, numerical simulations seem to fall within experimental uncertainty. Also, peak temperatures were simulated close to the interface between the preheating and combustion regions, a feature also observed in [24] when using the single-step global mechanism.

3.4. Effect of inlet velocity and excess air

Table 1 specifies values used for obtaining Fig. 4*a*, which presents results for a varying inlet mass flow rate, keeping unchanged all other parameters. Base reference values are those used in Case 03 of Pereira [14] (se also Table 1). As one can note in the figure, an increase in inlet velocity causes the increase of temperatures inside the burner. For small velocities up to $u_{in} = 0.20$ m/s, and consequently for low power conditions, diffusion and radiation transport smooth temperature gradients and interfacial heat transport decreases temperature difference between phases. As power inlet increases, gas temperature raises leading to distinct values for T_s and T_f in the combustion zone. Also, the equilibrium temperature is increased at the end of the burner. As the excess air is increased, Fig. 4*b*, temperature inside the burner increases, as expected. Also, for $\Psi < 0.54$ simulations indicate that combustion takes place in the preheating zone, a feature not desired in practical porous combustors.

3.5. Effect of porosity ϕ

In the figures to follow, both sections pictured in Fig. 1, namely the preheating and combustion regions, are investigated separately. Fig. 5*a* shows temperature profiles as a function of porosity ϕ in the preheating section. As more solid material per volume conducts more heat, temperature increases in the preheating section as ϕ decreases. Also, as a consequence of more heat being transported back to the inlet of the burner,

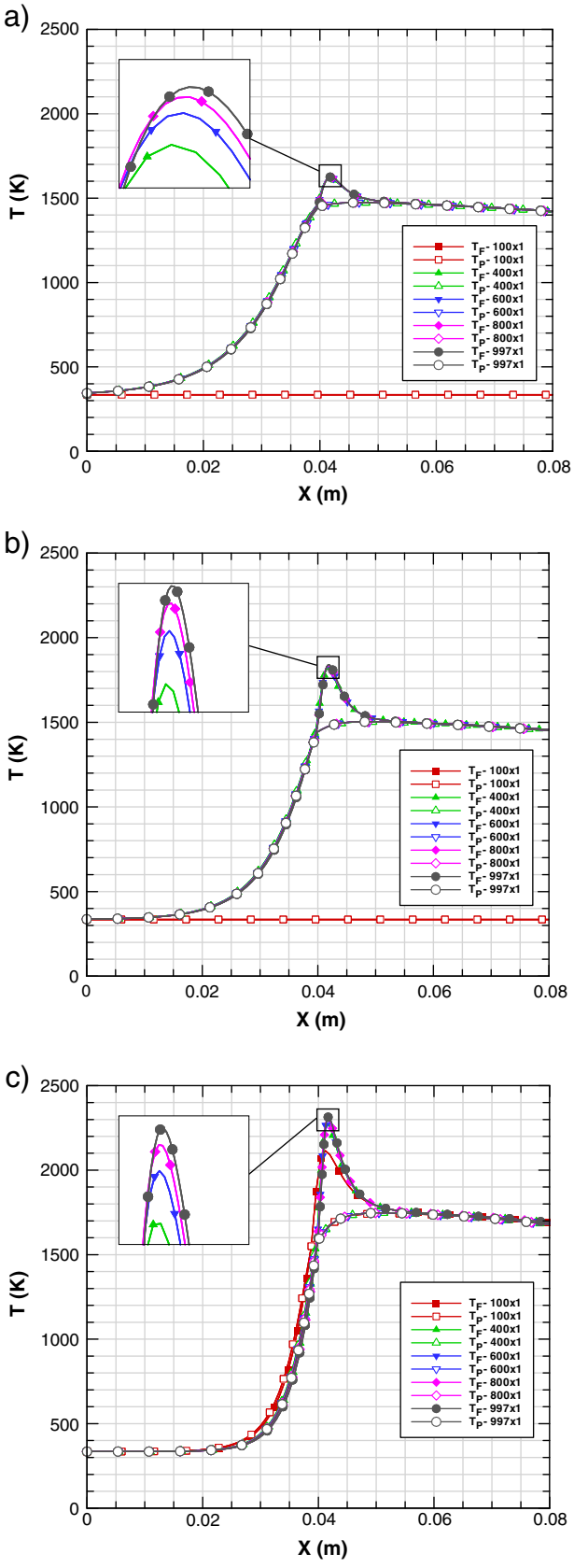

Fig. 2. Grid independency study for cases defined in Table 1: *a*) Case 01, $\Psi = 1.00$, $u_{in} = 0.15$ m/s; *b*) Case 02, $\Psi = 1.00$, $u_{in} = 0.21$ m/s); *c*) Case 03, $\Psi = 0.67$, $u_{in} = 0.40$ m/s.

peak gas temperatures are reduced in the combustion region ($x > 0.05$ m). Fig. 5*b* shows corresponding effects as porosity is varied in the combustion region. As porosity increases, peak gas temperatures

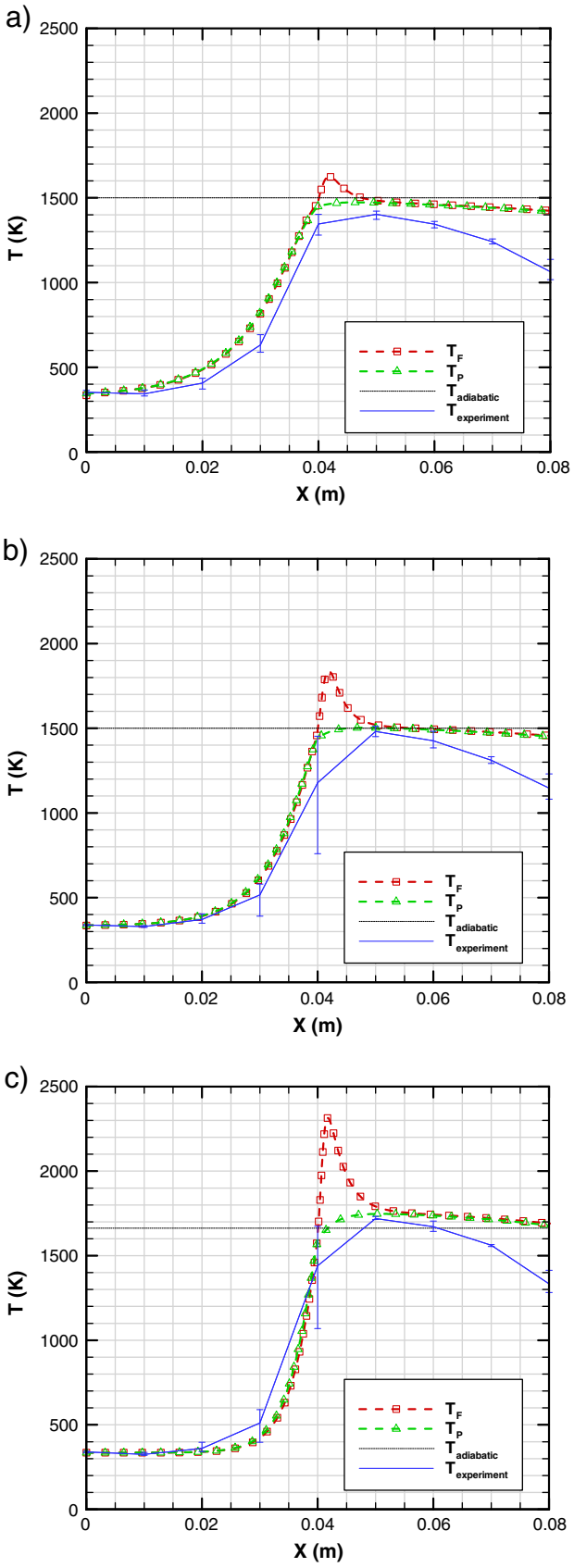

Fig. 3. Code validation and comparison with experiments by [14]: *a*) Case 01, $\Psi = 1.00$, $u_{in} = 0.15$ m/s; *b*) Case 02, $\Psi = 1.00$, $u_{in} = 0.21$ m/s); *c*) Case 03, $\Psi = 0.67$, $u_{in} = 0.40$ m/s.

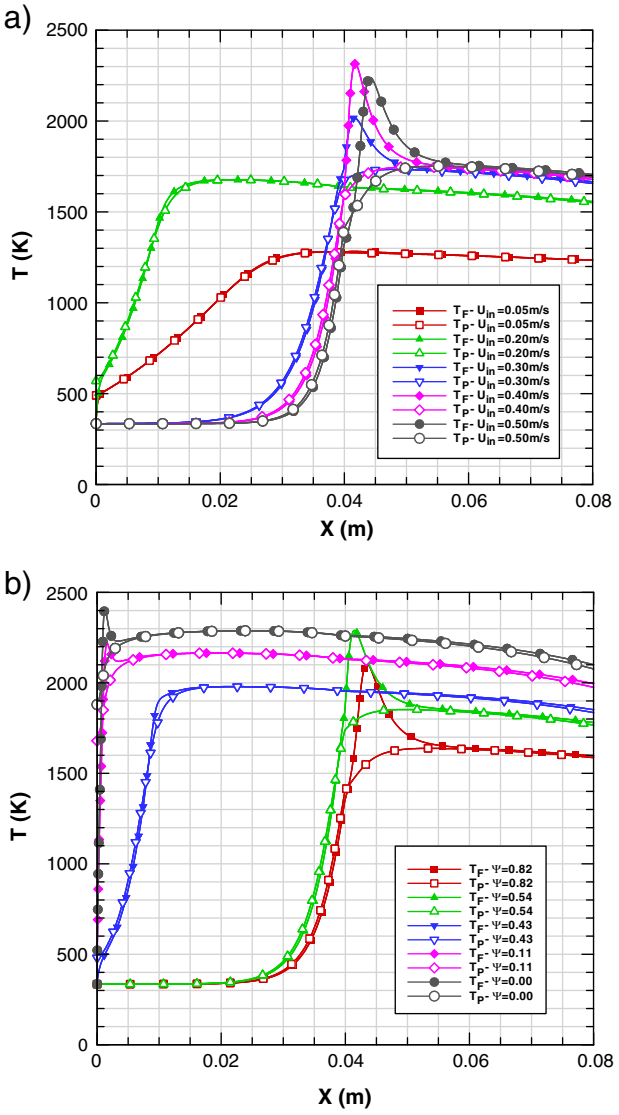

Fig. 4. Gas and solid temperatures: *a*) Effect on inlet gas velocity u_{in}, $\Psi = 0.67$; *b*) Effect of excess air Ψ, $u_{in} = 0.4$ m/s.

get closer to the interface between regions raising the solid temperature everywhere along the combustion section. Also, for high porosity materials, thermal equilibrium is achieved faster bringing the equilibrium position, where both temperatures equalize, closer to the beginning of the burning section. Further, outlet temperatures are higher for lighter and less dense materials.

3.6. Effect of k_s/k_f

Fig. 6 finally shows the effect of the solid-to-fluid thermal conductivity ratio. Increasing k_s/k_f in the preheating section (Fig. 6*a*) smoothes temperature gradients everywhere and eliminates the peak in the gas temperature inside the combustion region. In most practical applications, however, preheating sections are made of low conductivity material with not-to-high porosity in order to avoid flame flash back and loss of heat power at the burner exit [25].

For the combustion region, Fig. 6*b*, increasing of the solid-to-fluid conductivity ratio seems to cause little influence on the final temperature profiles. It is worth noting, however, that for value less than $k_s/k_f = 1560$ no ignition was achieved. In conclusion, one can mention that it is important to build the combustion region with high thermal conductivity

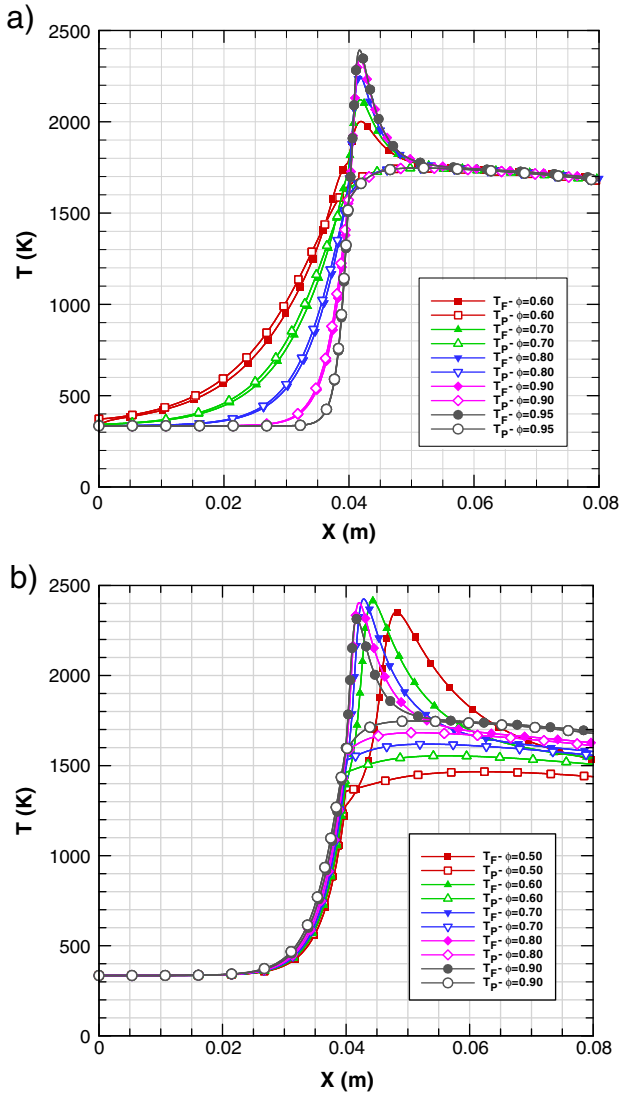

Fig. 5. Effect of φ on gas and solid temperatures: *a*) preheating region; *b*) combustion region.

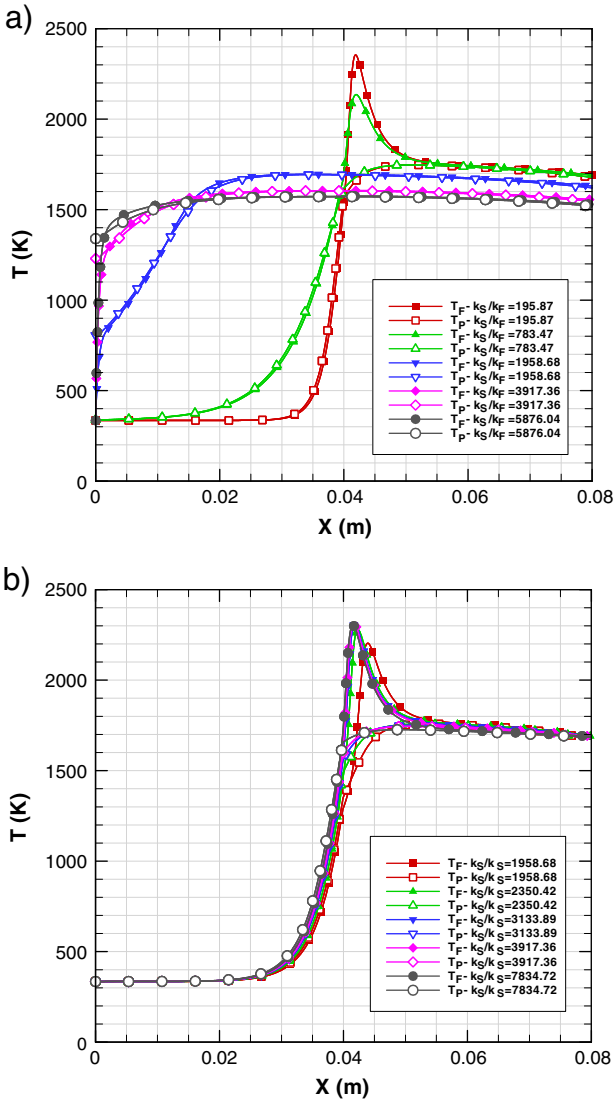

Fig. 6. Effect of k_s/k_f on gas and solid temperatures: *a*) preheating region; *b)* combustion region.

materials in order to enhance the regenerative process and heat recirculation within the burner, which, in turn, maintain high efficiency and allow the burning of low heating value gases [3].

4 . Concluding remarks

This paper expands previous work on combustion in porous media by validating simulations with available experimental data. The results indicate that increasing the mass flow rate, peak temperature increases, a result that follows similar trends observed in the experiments. For the geometry here analyzed, low excess air values will cause combustion in the preheating section, which is not desirable in practical applications. Low porosity values contribute to enhancing diffusion within the material, transporting heat toward the inlet and, as such, increasing heat recirculation and thermal efficiency of the porous combustor.

Acknowledgments

The authors are thankful to CNPq and CAPES, Brazil, for their financial support during the course of this research.

References

[1] J.R. Howell, M.J. Hall, J.L. Elzey, Combustion of hydrocarbons fuels within porous inert media, International Communications in Heat and Mass Transfer 37 (1996) 121–145.
[2] M. Weclas, Potential of porous medium combustion technology as applied to internal combustion engines, Journal of Thermodynamics (2010) (Article ID 789262, 39 p.).
[3] S. Wood, A.T. Harris, Porous burners for lean-burn applications, Progress in Energy and Combustion Science 34 (2008) 667–684.
[4] M.A. Mujebuu, M.Z. Abdullah, M.Z.A. Bakar, A.A. Mohamad, M.K. Abdullah, A review of investigations on liquid fuel combustion in porous inert media, Progress in Energy and Combustion Science 35 (2009) 216–230.
[5] S. Voss, R. Steinbrück, M. Kautz, E. Schieβwohl, M. Arendt, J.T. Felde, J. Volkert, D. Trimis, Premixed hydrogen–air combustion system for fuel cell systems, International Journal of Hydrogen Energy 36 (2011) 3697–3703.
[6] M.A. Mujeebu, M.Z. Abdullah, M.Z.A. Bakar, A.A. Mohamad, M.K. Abdullah, Applications of porous media combustion technology — a review, Applied Energy 86 (2009) 1365–1375.
[7] M.A. Mujeebu, M.Z. Abdullah, A.A. Mohamad, M.Z.A. Bakar, Trends in modeling of porous media combustion, Progress in Energy and Combustion Science 36 (2010) 627–650.
[8] P.-F. Hsu, W.D. Evans, J.R. Howell, Experimental and numerical study of premixed combustion within nonhomogeneous porous ceramics, Combustion Science and Technology 90 (1993) 149–172.
[9] M.J.S. de Lemos, Turbulence in Porous Media: Modeling and Applications, 1st ed. Elsevier, Amsterdam, 2006.
[10] M.J.S. de Lemos, Numerical simulation of turbulent combustion in porous materials, International Communications in Heat and Mass Transfer 36 (10) (2009) 996–1001.
[11] M.J.S. de Lemos, Analysis of turbulent combustion in inert porous media, International Communications in Heat and Mass Transfer 37 (4) (2010) 331–336.

[12] M.J.S. de Lemos, Simulation of turbulent combustion in porous materials with one- and two-energy equation models, in: A. Öchsner, G.E.E. Murch (Eds.), Heat Transfer in Multi-Phase Materials, Advanced Structured Materials, 2, Springer, Heidelberg, 2011, pp. 443–460.
[13] M.J.S. de Lemos, A.C. Pivem, Turbulent flow with combustion in a moving bed, International Communications in Heat and Mass Transfer 39 (1) (2012) 1–7.
[14] F.M. Pereira, Medição de Características Térmicas e Estudo do Mecanismo de Estabilização de chama em Queimadores Porosos Radiantes, Master's Thesis, Universidade Federal de Santa Catarina (*in Portuguese*), Florianópolis, Brazil (2002).
[15] S. Ergun, Fluid flow through packed columns, Chemical Engineering Progress 48 (2) (1952) 89–94.
[16] M.B. Saito, M.J.S. de Lemos, A correlation for interfacial heat transfer coefficient for turbulent flow over an array of square rods, Journal of Heat Transfer 128 (2006) 444–452.
[17] M.B. Saito, M.J.S. de Lemos, Interfacial heat transfer coefficient for non-equilibrium convective transport in porous media, International Communications in Heat and Mass Transfer 32 (5) (2005) 666–676.
[18] F. Kuwahara, M. Shirota, A. Nakayama, A numerical study of interfacial convective heat transfer coefficient in two-energy equation model for convection in porous media, International Journal of Heat and Mass Transfer 44 (2001) 1153–1159.
[19] A.A. Mohamad, S. Ramadhyani, R. Viskanta, Modelling of combustion and heat transfer in a packed bed with embedded coolant tubes, International Journal of Heat and Mass Transfer 37 (1994) 1181–1191.
[20] A.A. Mohamad, R. Viskanta, S. Ramadhyani, Numerical prediction of combustion and heat transfer in a packed bed with embedded coolant tubes, Combustion Science and Technology 96 (1994) 387–407.
[21] K.K. Kuo, Principles of Combustion, 2nd ed. John Wiley & Sons, New Jersey, 2005 (760 p.).
[22] S.R. Turns, An Introduction to Combustion: Concepts and Applications, 2nd ed. McGraw-Hill, New York, 2000 (704p.).
[23] K. Hanamura, R. Echigo, S.A. Zhdanok, Superadiabatic combustion in a porous medium, International Journal of Heat and Mass Transfer 36 (13) (1993) 3201–3209.
[24] X.Y. Zhou, J.C.F. Pereira, Comparison of four combustion models for simulating the premixed combustion in inert porous media, Fire and Materials 22 (1998) 187–197.
[25] A. Fuessel, H. Klemm, D. Boettge, F. Marschallek, J. Adler, A. Michaelis, Advancement of cellular ceramics made of silicon carbide for burner applications, IOP Conference Series: Materials Science and Engineering, 18, IOP Publishing Ltd., 2011.